An inversion approach for analysing the physical properties of a seismic low-velocity layer in the upper mantle

Jie Xiao[a, b, c,*], Saswata Hier-Majumder[b], Benoit Tauzin[d, e], Dave Waltham[b]

(a) State Key Laboratory of Organic Geochemistry, Guangzhou Institute of Geochemistry, Chinese Academy of Sciences, Guangzhou, 510640, China

(b) Department of Earth Sciences, Royal Holloway, University of London, Egham, TW20 0EX, United Kingdom

(c) University of Chinese Academy of Sciences, Beijing 100049, China

(d) Université de Lyon, UCBL, ENS Lyon, CNRS, Laboratoire de Géologie de Lyon, Terre, Planètes, Environnement, Villeurbanne, France

(e) Research School of Earth Sciences, Australian National University, Canberra, Australian Capital Territory 0200, Australia

* Corresponding author (xiaojie@gig.ac.cn)

16 **Abstract**

17   In this article, we propose a new inversion scheme to calculate the melt volume

18 fractions from observed seismic anomalies in a low-velocity layer (LVL) located atop

19 the mantle transition zone. Our method identifies the trade-offs in the seismic

20 signature caused by temperature, solid composition, melt volume fraction, and

21 dihedral angle at the solid-melt interface. Using the information derived from the

22 amplitude of *P*-to-*S* conversions beneath the western US, we show that the multiple

23 permissible solutions for melt volume fractions are correlated to each other. Any

24 possible solution can be directly transformed into alternative solutions whilst leaving

25 the model output unchanged. Hence, the additional solutions can be rapidly derived

26 given an initial solution. The calculation of multiple solutions reveals the universal

27 properties of the whole range of solutions. A regional-averaged melt volume fraction

28 of at least 0.5% occurs in every solution, even though a unique interpretation does not

29 exist.

30 **Keywords:** Shear wave, low-velocity layer, partial melting, inverse problem, non-

31 uniqueness

32

33 **1 Introduction**

34   The mantle transition zone (MTZ) – marked by a drastic change in the physical

35 properties of the silicate mineral phases – plays a crucial role in the convective flow of

36 the mantle. The sharp changes in density and volatile storage capacity across the

37 boundaries of the MTZ can act as impediments to mass transfer and as sites of partial

38 melting (Bercovici and Karato, 2003; Morra et al., 2010). Seismic observations also

39 provide evidence of partial melting atop the MTZ; a low-velocity layer (LVL) located at

40 ~350 km depth has been identified just above the mantle transition zone in numerous

41 regions around the world, with thickness from tens to a hundred kilometres (e.g. Song

42 et al., 2004; Gao et al., 2006; Courtier and Revenaugh, 2007; Schaeffer and Bostock,

43 2010; Tauzin et al., 2010; Huckfeldt et al., 2013). The 2 – 3% reductions in shear wave

44 velocities demarcate a sharp interface between the LVL and the overlying mantle,

45 indicating the likely presence of a chemical anomaly and, in particular, partial melting.

46 However, quantifying the fraction of melt has remained challenging because

47 environmental and chemical parameters, such as the mantle temperature, bulk solid

48 composition and melt geometry, are not clearly understood.

49   The LVL has frequently been interpreted as a small fraction of melt triggered by

50 volatile elements released from subduction zones (Revenaugh and Sipkin, 1994; Sun et

51 al., 2020) or mantle plumes (Vinnik and Farra, 2007). Since melts, characterized by zero

52 shear modulus, disproportionately reduce shear wave velocities, seismic anomalies

53 with low velocities are often qualitatively attributed to melting. Indirect evidence of

54 mass transfer between subducting slabs and surrounding mantle are obtained from

55 'superdeep diamonds' which bear geochemical signature of oxygen and carbon

56 isotopic ratios that can be generated by mixing between mantle and subducting slabs

57 at these depths.

58   The residual anomaly, defined as the difference between the observed shear

59 velocity and the reference velocity, can be attributed to the presence of melting and

60   used as a basis for calculating the volume fraction of melt in the LVL. Hence,

61   calculation of the melt fraction requires accurate estimation of the reference seismic

62   velocities, i.e. velocities in the absence of melting for given temperature and solid

63   composition. However, interpreting the origin of the seismic velocity anomalies in the

64   LVL is complicated by the competing influence of several additional factors. An

65   increase in temperature typically leads to seismic velocity reductions even without

66   melting whilst the influence of bulk mantle composition on seismic velocities varies

67   with depth (Xu et al., 2008). The multiple factors also likely affect each other.

68   Furthermore, melting may leave a strong impact on the bulk solid composition, in

69   particular the amount of basalt.

70   Non-uniqueness in LVL interpretations also arises from the fact that, in a partially

71   molten layer, the seismic velocity reductions depend on both the degree of melting

72   and the microstructure of the melt-bearing aggregates (Mavko, 1980; von Bargen and

73   Waff, 1986; Takei, 1998, 2002). The dihedral angle (also known as wetting angle) at the

74   solid-melt interface, controls the geometry of the load-bearing framework of partially

75   molten rocks (Hier-Majumder and Abbott, 2010), trading off with inferred melt volume

76   fraction. Chemical composition is also found to play a moderate role in reducing the

77   seismic speeds (Wimert and Hier-Majumder, 2012; Hier-Majumder et al., 2014), and

78   may alter the dihedral angle (Yoshino et al., 2005). The numerical experiment of Hier-

79   Majumder et al. (2014) indicated the difficulties in distinguishing different types of

80   melt from the seismic observations as the fraction of melt is very small.

81   A number of previous studies mitigated the issue of competing influences by

82   carrying out computationally expensive brute-force search to create lookup tables for

83   inferred melt volume fractions corresponding to different controlling factors (e.g. Hier-

84   Majumder and Courtier, 2011; Hier-Majumder et al., 2014; Hier-Majumder and Tauzin,

85   2017). While a brute-force search can produce a particular scenario of inversion,

86   application of the approach is unable to ascertain if alternative solutions exist in the

87   parameter space. Although, in principle, the entire range of solutions could be

88   discovered through repetitive use of the algorithm given different combinations of the

89   parameters, it fails to rigorously tackle the nature of variations in the inferred melt

90   volume fractions caused by changes in the other factors. Therefore, a new inversion

91   scheme is required to interpret these geophysical observations and to address the

92   theoretical drawback of previous studies.

93   Here we present a mathematical formulation that uses the implicit symmetry of a

94   petrologic model to understand the non-uniqueness in the melt fraction inference. The

95   principle of symmetry has been successfully applied in a sedimentological problem

96   (Xiao and Waltham, 2019), showing that multiple solutions can be closely linked even

97   when an inverse problem is non-linear. When symmetries exist, an existing solution

98   can be directly transformed into another solution that leaves modelling products

99   unchanged, in the same way that rotating a square by 90° produces an identical

100   geometry. In this way, the search for all possible solutions can begin with an initial

101   solution generated through standard inversion techniques. Application of the

102   symmetry method then allows additional solutions to be calculated from the initial

103   solution.

104   This paper uses the resultant inversion scheme to revisit the 350-km LVL beneath

105   the western US. A seismically anomalous layer in this region has been reported

106   underneath the Oregon-Washington border (e.g. Song et al., 2004; Tauzin et al., 2013),

107   Yellowstone (e.g. Fee and Dueker, 2004; Jasbinsek and Dueker, 2007), the Northern

108   Rocky Mountains (e.g. Jasbinsek and Dueker, 2007; Zhang et al., 2018), the Colorado

109   Plateau/Rio Grande Rift (e.g. Jasbinsek et al., 2010), and California (e.g. Vinnik et al.,

110   2010). Once the complete set of solutions has been derived, the lowest possible

111   fractions of melt within the LVL can be easily determined. As such, we can generate a

112   robust, lower-bound estimate of amount of partial melting in the LVL that does not

113   rely on assumed values of the other parameters. The calculation also offers more

114   reliable information about the solid mantle, such as the plausible ranges of

115   temperature and basalt fraction. For example, the estimates of melt content and

116   associated parameters can be used to infer the budget of volatile elements in the

117   mantle and the excess temperature of the mantle plumes beneath the region.

118

119   **2 The 350-km LVL beneath the western US**

120   *2.1 Seismic observations*

121   The seismic data used here are teleseismic *P*-to-*S* conversions recorded on

122   receiver functions from the Transportable Array of seismic stations in the western US

123   (fig. 1). Shear wave velocity contrasts at a depth of around 350 km have been derived

124   for 583 sites over a 0.5° × 0.5° grid in latitude and longitude. The seismically anomalous

125   layer covers an area of 1.8×10^6 km^2, with lateral thickness from 25 to 90 km (Tauzin et

126   al., 2013; Hier-Majumder and Tauzin, 2017).

127

128   *2.2 Calculating shear wave velocities*

129   To invert the shear wave speeds in the LVL from the seismic observations, we

130   follow the computational approach outlined in Hier-Majumder et al. (2014). We use

131   the results of mode-conversion amplitudes at the top and the base of the LVL to

132   estimate the velocity variations. To eliminate systematic variations in the amplitude of

133   converted arrivals caused by differences in seismic wave incidence, we normalize the

134   observed seismic amplitudes prior to computation. The normalized amplitude is

135   calculated from the ratio of amplitudes of arrivals converted at the top of the LVL over

136   arrivals converted at the olivine-wadsleyite mineralogical phase change at 410 km

137   depth:

$$R_{\mathrm{norm}} = \frac{A_{\mathrm{LVL}}}{A_{410}} < 0 \tag{1}$$

138   , where A_{LVL} is the frequency-averaged amplitude at the top of the LVL recorded at

139   each cell on the grid, and A_{410} is the frequency-averaged amplitude at the 410-km

140   discontinuity in the same cell. Using R_{norm}, we then calculate the shear wave velocity

141   (V_S^{obs}) at each location from the normalized contrast between the shear velocity

142   immediately above the 350-km LVL (V_S^{350}) and the velocity immediately below the

143   410-km discontinuity (V_S^{410}):

7

$$V_S^{\text{obs}} = V_S^{350}\left(1 + R_{\text{norm}}\frac{V_S^{410} - V_S^{350}}{V_S^{350}}\right) \tag{2}$$

144　We calculate V_S^{350} and V_S^{410} as the shear wave velocities at the depths of 350 km and

145　410 km, respectively, from the Preliminary Reference Earth Model (PREM, Dziewonski

146　and Anderson, 1981). Compared to the global predictions from the PREM (~4735 m/s

147　at 350 km depth), the estimated shear-velocities yield an average reduction of 1.6%.

148
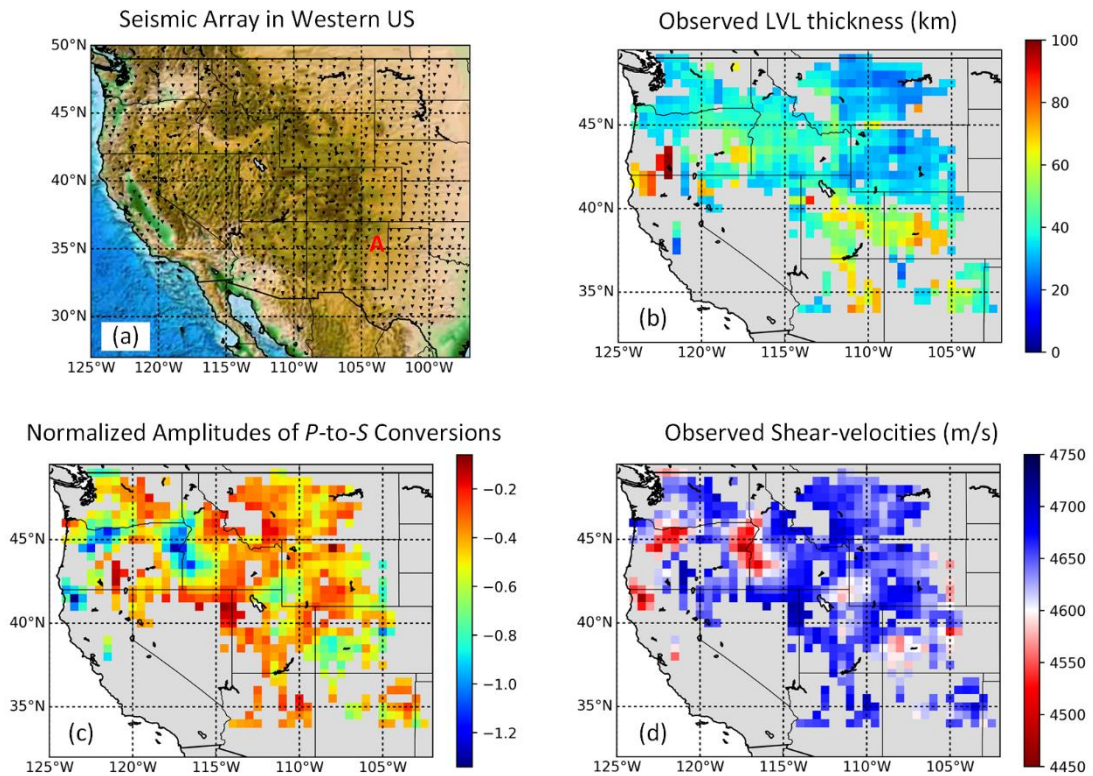
149

150　**Figure 1** Seismic observations of the 350-km LVL below the western US. (a) A map of the dense

151　seismic array of 820 sites (black triangles, from Tauzin et al., 2013). The seismic cell (106.5°W,

152　38°N) discussed later in this paper is labelled 'A'. (b) The thickness of the LVL beneath 583 sites

153　(from Hier-Majumder and Tauzin, 2017). (c) Normalized amplitudes of P-to-S converted arrivals. (d)

154　Shear wave velocities in the LVL estimated from the seismic data.

155

156   *2.3 Evaluating relative temperature variations*

157   We then evaluate the thermal variations in the LVL using the method outlined in

158   Tauzin and Ricard (2014). In this method, the temperature variations (ΔT) are related

159   to the observed thickness of the MTZ (δh) and the Clapeyron slopes (i.e. the change in

160   pressure of phase transition with respect to the change in temperature at which the

161   phase transition occurs) for the olivine-wadsleyite phase transitions at 410 km (γ_{410})

162   and 660 km (γ_{660}). We employ the data of spatial variations in MTZ thickness beneath

163   the western half of the US from Tauzin et al. (2013). We also set the reference MTZ

164   thickness at 250 km calculated by Tauzin and Ricard (2014) using the IASP91 spherical

165   model of Kennett and Engdahl (1991). We follow the empirical scheme of Tauzin and

166   Ricard (2014) and set γ_{410} = 3.0 MPa/K and γ_{660} = 0.64 γ_{410} − 1.17. The uncertainties

167   associated with the supplementary parameters will be discussed in later sections.

168   Using these methods, we calculate the temperature variations in the LVL from the MTZ

169   thickness beneath the seismic array (see fig. 2).

170
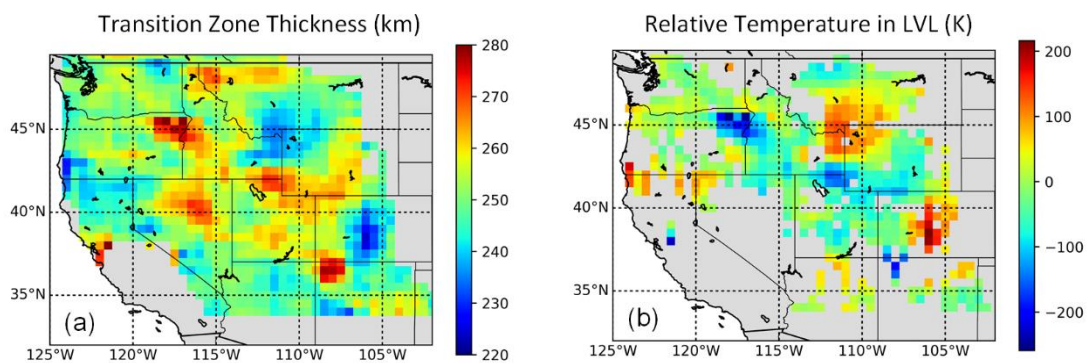
171

172   **Figure 2** Thickness of MTZ (a) and temperature variations in the LVL (b) estimated from the MTZ

173   thickness (after Tauzin and Ricard, 2014).

9

3 Forward modelling

The forward model of shear-velocities presented here incorporates four primary

controls, including the mantle potential temperature, bulk solid composition, melt

volume fraction and dihedral angle at the solid-melt interface. The simulation of shear

wave speeds in the LVL consists of two independent steps. Firstly, we estimate the

reference velocities from the properties of the solid mantle. Secondly, we calculate the

changes in velocities as waves travelling through a melt-bearing aggregate using a

micromechanical model that involves both the fraction and geometry of the melt.

3.1 Estimating reference velocities

We estimate the reference shear wave speeds in the solid mantle accounting for

the thermal and compositional properties of the mineral. The mantle temperature

below each site can be expressed as

$$T = T_0 + \frac{\mathrm{d}T}{\mathrm{d}z} z_{\mathrm{LVL}} + \Delta T \tag{3}$$

, where T_0 is the potential temperature of the reference mantle, $\mathrm{d}T/\mathrm{d}z$ is the

adiabatic temperature gradient which is suggested as $0.4 - 0.5$ K/km in the upper

mantle (Katsura et al., 2010), z_{LVL} is the depth of LVL and ΔT is the temperature

variation at a given location. We set z_{LVL} at the average depth of 352 km as observed

from the seismic profiles. To quantify the mantle composition, we follow the definition

from Xu et al. (2008) which parameterizes the mantle as a mechanical mixture of mid-

ocean ridge basalt and harzburgite. In this formulation, the composition of the solid

194   mantle can be expressed as the fraction of basaltic component. We can then formulate

195   the reference shear wave velocities as $V_S^{\text{ref}} = V_S^{\text{ref}}(T_0, C)$, where T_0 and C are the

196   potential temperature and basalt fraction of the mantle, respectively.

197   Reference shear wave speeds applied here are derived from the mineral physics

198   database of Xu et al. (2008), in which seismic velocities are tabulated with associated

199   combinations of potential temperatures and basalt fractions. In the database,

200   potential temperatures range from 1000 to 2000 K with increments of 100 K whereas

201   basalt fractions range from 0 to 100% with increments of 5%. While we can select a

202   given value of C for the calculation, the temperature at any point on the seismic grid is

203   determined from the MTZ thickness as discussed above. As a result, we interpolate the

204   value of seismic velocity for the temperature evaluated at each location using a

205   second-order polynomial interpolation between two tabulated values. Using this

206   interpolation, we are able to calculate the value of reference shear wave speed at each

207   point for a given bulk basalt volume fraction and a given reference potential

208   temperature. Figure 3 presents the predictions of regional-average shear wave speeds

209   for a range of potential temperatures and basalt fractions at a constant pressure of

210   11.7 GPa. The thermal and compositional effects can trade off each other and thus

211   different combinations of the two variables may lead to the same velocities.

212

Regional-averaged Reference V_S in LVL
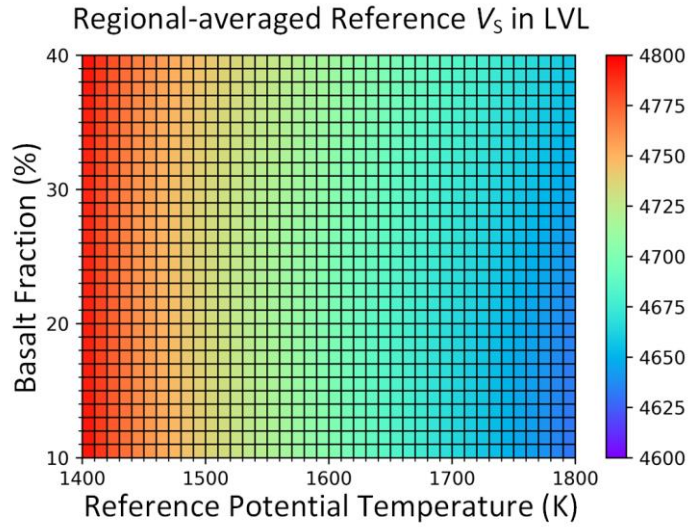
213

214 **Figure 3** Predicted regional-averaged reference shear wave velocities at 11.7 GPa in response to

215 different combinations of reference potential temperature and basalt fraction in the LVL beneath

216 the western US.

217

218 *3.2 Partial melting and velocity reductions*

219   To simulate the influence of partial melting on seismic velocities, we employ the

220 modelling scheme of Takei (2002), where the shear wave speed variation ξ is governed

221 by the effective elastic moduli of the aggregate:

$$\xi = \sqrt{\frac{N/\mu}{\bar{\rho}/\rho_{\mathrm{s}}}} \tag{4}$$

222 , where N is the effective shear modulus of the intergranular skeletal framework that

223 indicates the strength of contact between the neighbouring grains, μ is the shear

224 modulus of the solid devoid of a melt phase, ρ_s is the density of the solid bulk and $\bar{\rho}$ is

225 the volume-averaged density of the entire aggregate which is calculated as:

$$\bar{\rho} = \rho_{\mathrm{m}}\varphi + \rho_{\mathrm{s}}(1 - \varphi) \tag{5}$$

226 , where ρ_m is the density of the melt; φ is the volume fraction of melt within the

227 aggregate.

228 In Eq. (4), the elastic modulus N is determined by both the melt volume fraction φ

229 and the contiguity (ψ, i.e. the area fraction of the intergranular contact) of the melt:

$$N = \mu(1 - \varphi)[1 - (1 - \psi)^n] \tag{6}$$

230 The contiguity ψ depends on the melt volume fraction φ and the dihedral angle θ

231 between the solid grains and the melt; and n is an exponent also depending on ψ

232 (Takei, 2002). The simulations of contiguity applied here are based on the micro-

233 structural model of von Bargen and Waff (1986) which formulates the contiguity ψ as

234 the proportion that the contact area of grains occupy among the total contact area in a

235 partial molten aggregate:

$$\psi = \frac{2A_{\text{gg}}}{2A_{\text{gg}} + A_{\text{gm}}} \tag{7}$$

236 , where A_{gg} and A_{gm} are the grain-grain contact area and grain-melt contact area per

237 unit volume, respectively. The values of A_{gg} and A_{gm} are calculated from the given

238 melt volume fraction and dihedral angle using polynomial functions:

$$\begin{cases} A_{\text{gg}} = \pi - b_{\text{gg}}\text{power}(\varphi, p_{\text{gg}}) \\ A_{\text{gm}} = b_{\text{gm}}\text{power}(\varphi, p_{\text{gm}}) \end{cases} \tag{8}$$

239 The required constants b_{gg}, b_{gm}, p_{gg} and p_{gm} are approximated from quadratic

240 polynomials of the dihedral angle (in degree), of which the values are outlined in von

241 Bargen and Waff (1986). Wimert and Hier-Majumder (2012) demonstrated this

242 approximation of contiguities can produce satisfactory fits with experimental

243 measurements from partially molten aggregates with melt volume fractions below 5%.

244   Combining Eqs. (3) – (7) enables the contiguity to be expressed as a function of the

245 melt volume fraction φ and dihedral angle θ, i.e. $\psi = \psi(\varphi, \theta)$. Moreover, shear wave

246 speed anomalies ξ caused by partial melting can be formulated as a function with

247 respect to melt volume fraction and dihedral angle:

$$\xi(\varphi, \theta) = \sqrt{\frac{(1 - \varphi)\left[1 - \left(1 - \psi(\varphi, \theta)\right)^{n}\right]}{1 - \varphi(1 - \rho_{\mathrm{m}}/\rho_{\mathrm{s}})}} \tag{9}$$

248 We estimate the densities of solid bulk ρ_s and melt ρ_{m} using the third-order Birch-

249 Murnaghan equation of state (EOS), as Ghosh et al. (2007) suggested for carbonated

250 peridotite melt. We implement the mathematic approximations using MuMaP_fwd

251 (Hier-Majumder, 2017), a Python computational toolkit for microscale geodynamic

252 study. The modelled shear wave velocity reductions in response to a variety of melt

253 volume fractions and dihedral angles are illustrated in fig. 4. The curves show that the

254 velocity in the partially molten aggregates decreases rapidly as the fraction of melt

255 increases. The curves also show that, for the same melt volume fraction, a smaller

256 dihedral angle results in greater reductions in the shear wave speed. Hence, different

257 combinations of dihedral angles and melt volume fractions produce the same shear-

258 velocity reductions.

259
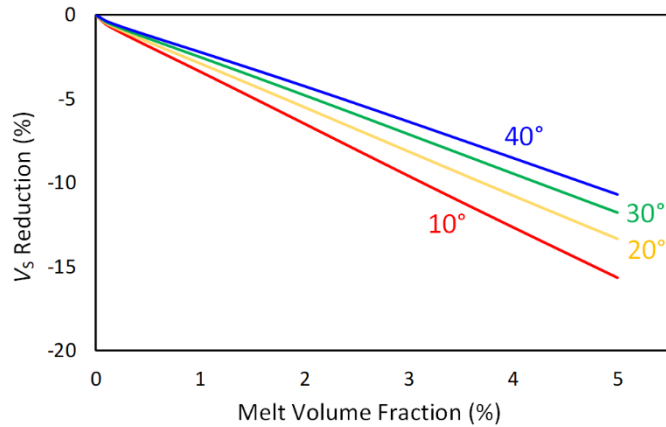
Figure 4 Predicted shear wave velocity reductions for different melt volume fractions and dihedral

angles. Each curve shows the velocity reductions caused by changes in melt volume fraction at the

indicated dihedral angle.

4 Model inversion

The forward modelling approach described in the preceding section predicts the

shear wave velocity reductions in response to associated parameters. Alternatively, it

is possible to calculate the velocity reductions as a ratio of the observed velocity over

the reference velocities:

$$\xi = \frac{V_S^{\text{obs}}}{V_S^{\text{ref}}(T_0, C)} \tag{10}$$

When embedded with an inversion scheme, the numerical model can be used to

deduce the controls on seismic velocities. The inversion procedure can begin with an

initial solution that is built upon petrologic and seismological constraints. We then

investigate how to exploit and utilize the symmetry of the model, which can allow us

to alter the initial solution directly into another solution whilst giving the same

275   observations. In this way, the additional solutions to the inverse problem can be

276   rapidly derived by repeated use of the transformation.

277

278   *4.1 An initial solution based on a priori knowledge*

279   To incorporate the forward model and the observed data in a single framework,

280   we firstly combine Eqs. (9) and (10):

$$\sqrt{\frac{(1-\varphi)\cdot\left[1-\left(1-\psi(\varphi,\theta)\right)^n\right]}{1-\varphi(1-\rho_\mathrm{m}/\rho_\mathrm{s})}} = \frac{V_\mathrm{S}^\mathrm{obs}}{V_\mathrm{S}^\mathrm{ref}(T_0,C)} \tag{11}$$

281   , which gives four unknowns (i.e. T_0, C, θ and φ) in one equation. To solve for melt

282   volume fraction φ from Eq. (11), the reference potential temperature T_0, basalt

283   fraction C and dihedral angle θ need to be specified. We initially assume the reference

284   potential temperature to be 1500 K in the region. We set the basalt fraction at 18%, as

285   suggested in Xu et al. (2008) for common peridotite. The dihedral angle at the grain-

286   melt interface varies with the chemical composition of the melt. For example, Minarik

287   and Watson (1995) proposed dihedral angles varying from 25 to 30° at the interface

288   between carbonate melt and molten aggregates; Mei et al. (2002) suggested a dihedral

289   angle of 28° for molten aggregates with hydrous basalt melt. Here we initially assume a

290   dihedral angle of θ = 25°. Given these *a priori* assumptions, T_0, C and θ are specified,

291   and hence the melt volume fraction can be solved from Eq. (11).

292   We then calculate the corresponding melt volume fraction φ using a modified

293   Newton-Raphson root-search algorithm (Press et al., 2007, chap. 9.1), as previously

294   demonstrated by Hier-Majumder and Tauzin (2017). The algorithm begins with a

295   bracket for the melt volume fraction between 1×10^{-4}% and 10% and iterates the

296   searching process until a convergence of 10^{-4}% is achieved in the inferred fraction.

297   Figure 5 shows the initial solution derived from the inversion using the seismic

298   observations and the constraints on T_0, C and θ. The melt fractions in the region vary

299   spatially and yield an average of 0.72%. As a check, synthetic velocities reproduced

300   from the forward model (fig. 5c) are a good match to the original observations (fig. 1d).

301
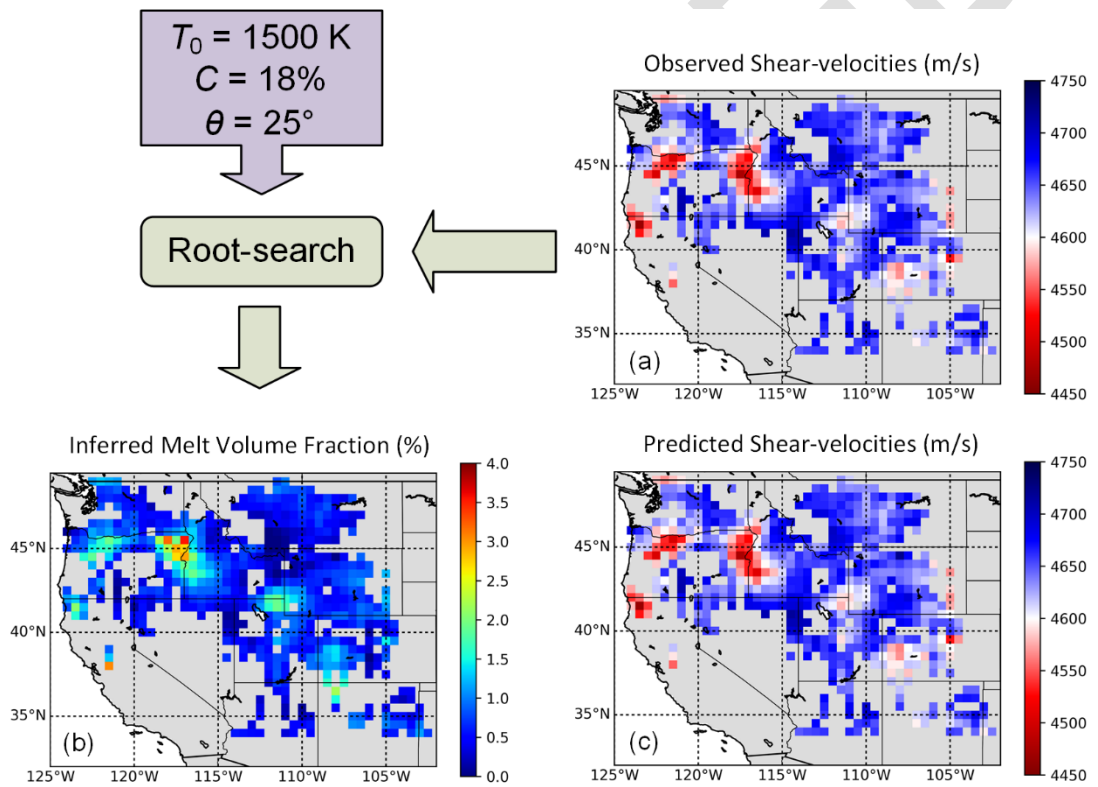
302

303   **Figure 5** An initial solution to the inverse problem of the 350-km LVL. The observed shear wave

304   velocities (a) and reference values of T_0, C and θ are used to provide constraints on the inversion.

305   A particular solution for the melt vol% within the LVL (b) is then generated using the root-search

306   approach. The regionally averaged fraction is calculated as 0.72% for T_0 = 1500 K, C = 18% and θ =

307   25°. Using the inferred melt vol% and the reference values, shear wave velocities (c) can be

308   reproduced from the forward model.

309

310   *4.2 Symmetric transformation*

311   The above calculation generates a single solution to the inverse problem. Since the

312   inverse problem is non-unique with respect to the input parameters T_0, C and θ, there

313   are, in principle, an infinite number of alternative solutions that can reproduce

314   identical seismic observations. Here we develop a quantitative approach to prove the

315   non-uniqueness and, more crucially, the transformation from an existing solution to an

316   alternative solution. The symmetry of the numerical model is found by modifying the

317   input parameters to obtain an unchanged output model. To start with, we formulate

318   the forward model of shear wave speed as:

$$\boldsymbol{V}_S = F(T_0, C, \theta, \boldsymbol{\varphi}) \tag{12}$$

319   , where $\boldsymbol{V}_S$ is the shear wave speeds in the LVL beneath the seismic sites; F denotes a

320   general, non-linear function (in this work, F is the forward model from the code

321   MuMaP_fwd) and $\boldsymbol{\varphi}$ is a vector of melt volume fractions in the LVL. Note that 583

322   seismic sites are analysed in this study, and hence the vector lengths are 583 for both

323    $\boldsymbol{V}_S$ and $\boldsymbol{\varphi}$. We then generate three perturbations δT_0, δC and $\delta\theta$. These small changes

324   in the model inputs give rise to residuals in the modelled velocities, i.e. $\Delta\boldsymbol{V}_S$. This can

325   be written as:

$$\Delta\boldsymbol{V}_S = F(T_0 + \delta T_0, C + \delta C, \theta + \delta\theta, \boldsymbol{\varphi}) - F(T_0, C, \theta, \boldsymbol{\varphi}) \tag{13}$$

326 , which may be approximated in a linear form using the first-order Taylor's series:

$$\frac{\partial F}{\partial T_0}\delta T_0 + \frac{\partial F}{\partial C}\delta C + \frac{\partial F}{\partial \theta}\delta\theta = \Delta \boldsymbol{V}_S \qquad (14)$$

327 , where $\partial F/\partial T_0$, $\partial F/\partial C$ and $\partial F/\partial \theta$ are finite derivatives of the function F with

328 respect to T_0, C and θ. We then calculate changes required in the melt volume

329 fractions (i.e. $\delta\boldsymbol{\varphi}$) to compensate the changes in velocities resulting from the

330 perturbations. This can be expressed as:

$$F(T_0 + \delta T_0, C + \delta C, \theta + \delta\theta, \boldsymbol{\varphi} + \delta\boldsymbol{\varphi}) - F(T_0, C, \theta, \boldsymbol{\varphi}) = \boldsymbol{0} \qquad (15)$$

331 Approximation based on the Taylor's series gives:

$$\frac{\partial F}{\partial T_0}\delta T_0 + \frac{\partial F}{\partial C}\delta C + \frac{\partial F}{\partial \theta}\delta\theta + \frac{\partial F}{\partial \boldsymbol{\varphi}}\delta\boldsymbol{\varphi} = \boldsymbol{0} \qquad (16)$$

332 , where $\partial F/\partial\boldsymbol{\varphi}$ is the finite derivative of the function F with respect to $\boldsymbol{\varphi}$. We then

333 solve $\delta\boldsymbol{\varphi}$ by combining Eq. (14) and (16):

$$\delta\boldsymbol{\varphi} = -\frac{\Delta\boldsymbol{V}_S}{\partial F/\partial\boldsymbol{\varphi}} \qquad (17)$$

334 In this equation, $\partial F/\partial\boldsymbol{\varphi}$ can be calculated from the forward model. The new solution

335 can then be used as a basis for another transformation. Iterative transformation can

336 therefore derive all the additional solutions to the inverse problem.

337

338 *4.3 Calculating multiple solutions*

339 Using the forward model and symmetric transformation, we then examine the

340 entire parameter space and calculate alternative solutions. The parameter space can

341 be considered as a 3-D space with basis vectors potential temperature (T_0), basalt

342 fraction (C) and dihedral angle (θ). We define the ranges of the parameters as 1400 to

343 1800 K in potential temperature, 10 to 40% in basalt fraction and 10° to 40° in dihedral

344 angle. We also set the increments at 10 K in potential temperature, 1% in basalt

345 fraction and 1° in dihedral angle, sampling the parameter space in small intervals. Each

346 position in the parameter space can be described using the coordinates in the 3-D

347 space. If a solution exists in position (T_0, C, θ), then the corresponding melt volume

348 fraction vector can be written as $\boldsymbol{\varphi}(T_0, C, \theta)$. Once a solution is found, the solutions in

349 neighbouring positions can also be determined. Because the transformation can be

350 applied both forward and backward, six neighbouring solutions should be examined,

351 including $\boldsymbol{\varphi}(T_0 + \delta T_0, C, \theta)$, $\boldsymbol{\varphi}(T_0 - \delta T_0, C, \theta)$, $\boldsymbol{\varphi}(T_0, C + \delta C, \theta)$, $\boldsymbol{\varphi}(T_0, C - \delta C, \theta)$,

352 $\boldsymbol{\varphi}(T_0, C, \theta + \delta\theta)$ and $\boldsymbol{\varphi}(T_0, C, \theta - \delta\theta)$. We calculate the additional solutions through

353 the following procedure:

354 (1) Create an empty list. Add the coordinate of the initial solution into the list.

355 (2) For each solution in the list, calculate the solutions in the neighbouring

356   positions that are inside of the parameter space but not existing in the list.

357 (3) Add the solutions found in step (2) into the list.

358 (4) Return to step (2) and repeat the workflow until no new solution can be

359   added into the list.

360 Note that this is different from a brute-force search which involves a root-searching

361 approach for calculating the melt volume fraction beneath every location given

362 different combinations of T_0, C and θ. In contrast, the symmetric transformation is

363   straightforward as it can simultaneously derive the melt volume fraction beneath the

364   whole area. Since this method works directly on the behaviour of the solution with

365   respect to perturbations, it also allows us to predict regions where melting does not

366   exist and to predict the solution containing the lowest possible average melt fractions,

367   which was intractable with the method described by Hier-Majumder et al. (2014).

368

369   *4.4 Complete solutions to the inverse problem*

370   Using the above computational procedure, we derive all the solutions in the

371   parameter space. All the possible solutions can reproduce the same synthetic shear

372   wave velocities from the forward model. Significant spatial variations in the inverted

373   melt volume are found in every solution. Because the melt volume fraction should

374   always be non-negative, the calculated vectors of $\boldsymbol{\varphi}$ where one or more negative

375   values exist should be excluded. Given this requirement, limits can be placed to bound

376   the symmetric transformation, i.e. not every combination of potential temperatures,

377   basalt fractions and dihedral angles in the parameter space requires the presence of

378   melting to explain the seismic anomaly. Example of the variations in calculated melt

379   volume fractions and the transformation limits in the multiple controlling factors are

380   demonstrated in fig. 6.

381
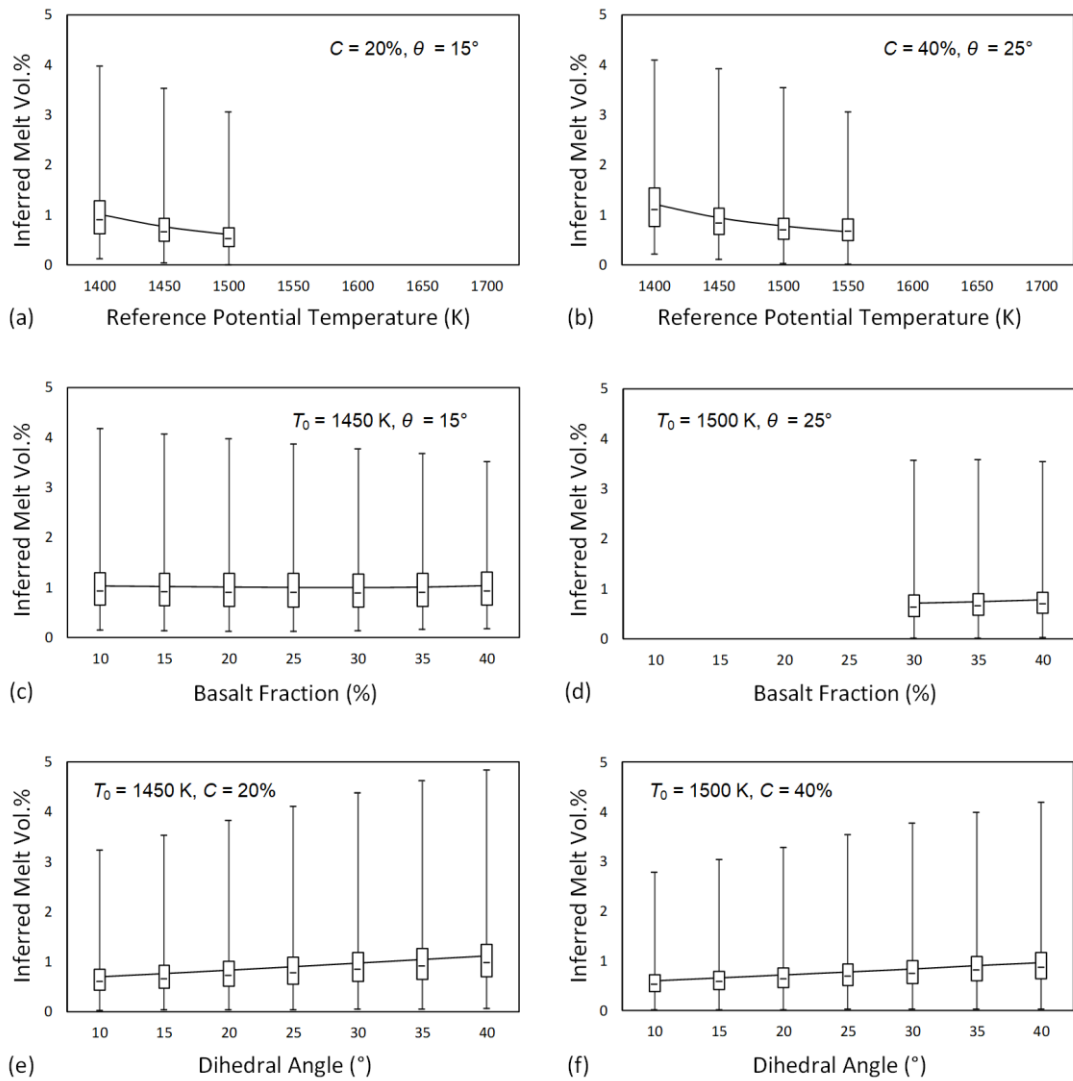
Figure 6 Estimated melt volume fractions beneath all locations with median indicated by the horizontal line within each box, upper/lower quartiles indicated by the upper/lower edges of the box and maximum/minimum indicated by whiskers of the boxes. (a) & (b) Inferred melt vol% as a function of reference potential temperature with fixed basalt fraction and dihedral angles. (c) & (d) Inferred melt vol% as a function of basalt fractions with fixed reference potential temperature and dihedral angle. (e) & (f) Inferred melt vol% as a function of dihedral angle with fixed reference potential temperature and basalt fractions. Note that no solution can be found given $T_0 \geq 1500$ in (a), $T_0 \geq 1550$ K in (b) and $C \leq 30\%$ in (d).

392   The model output illustrated in fig. 7 is an end-member solution showing that the

393   lowest possible averaged melt volume fraction is 0.51%, associated with T_0 = 1550 K, C

394   = 40% and θ = 10°. In this solution, melting is not predicted beneath some regions, for

395   instance at the triple border between Idaho, Montana and Wyoming. Considering the

396   sharp boundary atop the LVL, this may just be an artefact because the variations in

397   solid bulk are unlikely to produce rapid velocity reductions. However, this solution is

398   still meaningful since it places a lower-bound below the regional-averaged melt

399   volume fraction within the observed LVL. In contrast, the highest possible averaged

400   melt volume fraction that exists in the parameter space yields 1.47%, associated with

401   T_0 = 1400 K, basalt fraction C = 10% and dihedral angel θ = 10°, as shown in fig. 8.

402   Examples of the trade-offs between the estimated melt volume fraction below a given

403   location and the multiple controls are displayed in fig. 9 by cross-plotting the estimates

404   and the corresponding controlling factors. Whilst the forward model used here is non-

405   linear, application of the proposed method has indicated the trajectories that link

406   together the multiple solutions in the parameter space.

407

T_0 = 1550 K
C = 40%
θ = 10°

Inferred Melt Volume Fraction (%)

Predicted Shear-velocities (m/s)

(a)

(b)
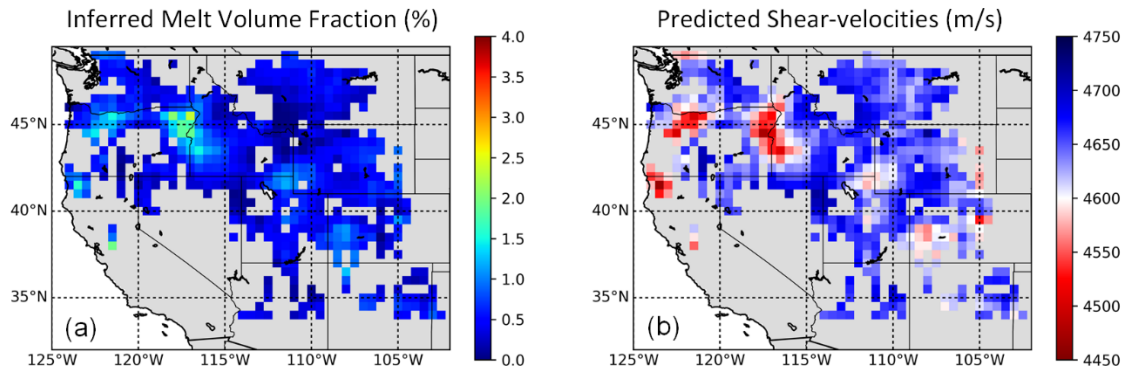
Figure 7 An end-member solution with the minimum melt vol% within the LVL beneath the western
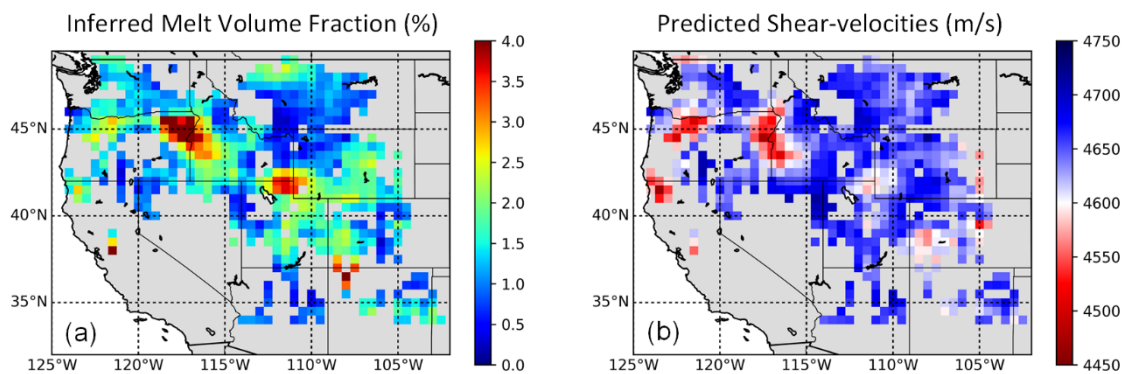
US. The regional averaged melt vol% is 0.51% given T_0 = 1550 K, C = 40% and θ = 10°. Note that this

solution is directly derived from the initial solution, rather than from a brute-force search.

T_0 = 1400 K
C = 10%
θ = 40°

Inferred Melt Volume Fraction (%)
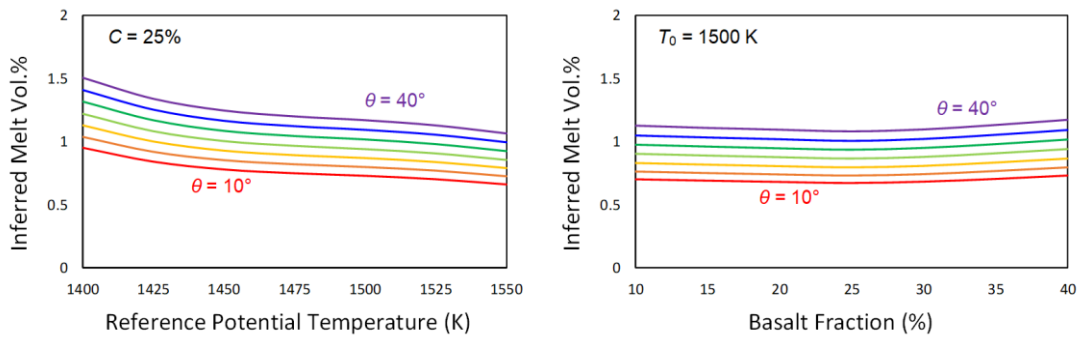
Predicted Shear-velocities (m/s)

(a)

(b)

Figure 8 An end-member solution with the maximum melt vol% within the LVL beneath the region.

The regional averaged melt vol% is 1.47% given T_0 = 1400 K, C = 10% and θ = 40°. Note that this

solution is directly derived from the initial solution, rather than from a brute-force search.

Figure 9 Inferred melt volume fractions beneath 106°W, 35°N (label 'A' in fig. 1a) versus (a) the reference potential temperature for different dihedral angles ranging from 10° to 40° with constant intervals of 5° given a fixed basalt composition and (b) the basalt fraction in the bulk composition for a range of different dihedral angles given a fixed potential temperature.

5 Discussion

Using a numerical inversion approach, we have examined the LVL at 350 km underneath the western US. The shear-velocity anomalies and impedance contrasts in this zone are thought to indicate a small fraction of volatile-rich melt (Hier-Majumder and Tauzin, 2017) released either by decarbonation during the Farallon slab subduction (Thomson et al., 2016) or by dehydration from the upwelling of the Yellowstone mantle plume or small-scale convection within the MTZ (Bercovici and Karato, 2003; Richard and Bercovici, 2009; Zhang et al., 2018). Despite the presence of petrological and geochemical evidences of melting near the MTZ, determination of the quantity of melting from seismic signatures remains challenging owing to the trade-offs that exist between various controlling factors. Due to the lack of geophysical and geochemical constraints, it is difficult, if not impossible, to distinguish the individual

25

435   effects of temperature, composition and partial melting. A recent study has further

436   suggested that these multiple controls are strongly correlated, leading to a

437   disagreement between experimental measurements and theoretical estimates (Freitas

438   et al., 2019).

439   Our numerical scheme based on a symmetry is able to cover all solutions. Using a

440   forward model, we firstly generate an arbitrary solution assuming T_0 = 1500 K, C = 18%

441   and θ = 25°. This is a successful solution as the shear wave velocities it predicts are

442   consistent with the observations. The inverse problem is then linearized to find

443   neighbouring solutions to the initial solution. As the controlling parameters have only a

444   limited range of plausible values (in this work 1400 ≤ T_0 ≤ 1800 K, 10% ≤ C ≤ 40% and

445   10° ≤ θ ≤ 40°), the symmetry gives a quasi-complete set of solutions subject to the

446   necessary constraint that the melt volume fraction in the upper mantle must always be

447   non-negative. This constraint can be justified as the effects of temperature and

448   composition are already taken into account. Given the above treatment, it is then a

449   simple matter to find the combinations of parameters that reveals the end-member

450   possibilities (e.g. maximum and minimum degrees of partial melting).

451   The modelling results show that a regional-averaged melt volume fraction of at

452   least 0.51% is necessary to explain the sharp shear-velocity reductions at 350 km

453   beneath the western US. This is the minimum extent of melting required to produce

454   the observed LVL, whatever the solid mantle conditions and the geometry of the melt

455   are. As no solution has been found to be associated with a reference potential

456   temperature higher than 1550 K, this is an upper-bound on the variations in the

457 reference potential temperature. The modelling output also shows that the range of

458 variations in basalt fraction depends on the assumed reference potential temperature.

459 At a low reference potential temperature (e.g. 1400 K), the basalt fraction may vary

460 from 10% to 40%. In contrast, at a higher reference potential temperature, solutions

461 can only be in the basaltic-rich zone (e.g. fig. 6d). For instance, Hier-Majumder and

462 Tauzin (2017) estimated the reference potential temperature as approximately 1550

463 K. If this is the case, then we can make a statement that the basalt fraction in the LVL

464 beneath the western US is no less than 40%. Hence, whilst the thermal and

465 compositional conditions are still under-constrained, our model work offers more

466 reliable information about mantle physical properties.

467   In addition, our inverse method unravels trade-offs between parameters. As the

468 forward model is nonlinear, there is no simple analytical tool for determining these

469 competing effects. The numerical approach proposed here estimates the rates of

470 change in the inferred melt volume fraction caused by changes in other parameters.

471 The trade-offs between inferred melt volume fractions and other parameters can be

472 summarized as:

473   (1) For a given dihedral angle and a given basalt fraction, the inferred melt

474   volume fractions show a negative correlation with the assumed reference

475   potential temperatures (fig. 6a & b).

476   (2) For a given reference potential temperature and a given dihedral angle, the

477   inferred melt volume fractions are insensitive to the assumed basalt fractions

478   (fig. 6c & d).

479   (3) For a given reference potential temperature and a given basalt fraction, the

480   inferred melt volume fractions show a modest positive correlation with the

481   assumed dihedral angles (fig. 6e & f).

482   Another issue that needs to be addressed while deducing the physical properties

483 of the LVL arises from the estimation of spatial variations in temperatures. This study

484 calculates the temperature variations from the thickness of the MTZ using the

485 empirical correlation proposed by Tauzin and Ricard (2014). The empirical model relies

486 on several assumptions, for example that only temperature controls MTZ thickness

487 and that no vertical variation occurs in temperature from the MTZ to the LVL. As

488 observed from tomographic models (with low vertical resolution), the MTZ has

489 consistent structures over the whole range of depth, in particular the stalled Juan de

490 Fuca/Farallon slab (Burdick et al., 2008; Schmandt et al., 2011; Hier-Majumder and

491 Tauzin, 2017). Although entirely consistent temperatures across the MTZ should not be

492 expected, dealing with the absolute topography of discontinuities to infer the

493 temperatures would likely introduce more uncertainties, and would require a precise

494 correction of the effect of shallow velocity heterogeneities from 3-D tomographic

495 models, which have their own limitations. Another assumption involved here is that

496 one can extract reliable MTZ thickness from receiver functions, while seismic phase

497 interference effects on the imaged structure at the base of MTZ can be neglected. In

498 fact, the move-out of interfering phases at the base of the MTZ is rather different from

499 the one from direct conversions (Guan and Niu, 2017). Stacking along move-out curves

500 for direct conversions is efficient in removing the effect of these interfering phases.

501   Besides, slant-stack diagrams and slowness weighted stacking (e.g. Guan and Niu,

502   2017; Hier-Majumder and Tauzin, 2017) show no evidence for any potential

503   interference effects in several locations of the western US. As a consequence, the

504   assumptions applied in the empirical model are tenable for calculating the

505   temperature variations in the LVL.

506   Apart from the primary controls on the seismic velocities we have investigated,

507   there are other factors that can influence the seismic wave speeds. In this work, the

508   Clapeyron slopes γ are set to values from a compilation of experimentally obtained

509   values (Tauzin and Ricard, 2014). The values of matrix density ρ_s and melt density ρ_m

510   are set to constants as suggested in previous studies. The thickness of MTZ applied

511   here are also from supplementary dataset whereas alternative empirical models (e.g.

512   Keifer and Dueker, 2019) would produce different scenarios. These additional

513   complications can lead to substantial uncertainties in estimated melt volume fractions.

514   However, the inversion technique presented here is independent from the forward

515   model and can easily be adapted to include these factors. While in this paper the

516   application of the inversion has been demonstrated using 1-D column simulation, the

517   technique could be applied to more sophisticated models that are spatially 2-D or 3-D.

518   For future work, we intend to apply our modelling approach to investigating the LVL

519   identified in other regions that differ in tectonic settings, for example, the Hawaii

520   Islands (Huckfeldt et al., 2013) which are dominated by mantle plumes.

521

522   **6 Conclusions**

523   The interpretation of the observed seismic structures in the upper mantle, like

524 many other geophysical inverse problems, is hampered by the fundamental challenge

525 of non-uniqueness. In this work, we investigate the influence of thermal,

526 compositional and melting effects on the pervasive LVL at 350 km beneath the western

527 US. We develop an inversion scheme, based on the principle of symmetry, for

528 generating the full range of solutions in the parameter space. Although a unique

529 solution is not present, the calculation of an ensemble of solutions allows extraction of

530 the properties that are common to all solutions. A key result of our inversion is that a

531 minimum fraction of ~0.5% melt by volume is necessary to explain the seismically

532 anomalous layer in the region. The scheme also encapsulates the ranges of variations

533 in the thermal and compositional factors. Consequently, the application of the

534 proposed inversion technique can provide more robust interpretation of seismic

535 velocity reductions within the mantle.

536

545   **References**

546   Bercovici, D., Karato, S.-i., 2003. Whole-mantle convection and the transition-zone

547   water filter. Nature 425, 39.

548   Burdick, S., Li, C., Martynov, V., Cox, T., Eakins, J., Mulder, T., Astiz, L., Vernon, F.L.,

549   Pavlis, G.L., van der Hilst, R.D., 2008. Upper mantle heterogeneity beneath

550   North America from travel time tomography with global and USArray

551   transportable array data. Seismological Research Letters 79, 384-392.

552   Courtier, A.M., Revenaugh, J., 2007. Deep upper-mantle melting beneath the Tasman

553   and Coral Seas detected with multiple ScS reverberations. Earth and Planetary

554   Science Letters 259, 66-76.

555   Dziewonski, A.M., Anderson, D.L., 1981. Preliminary reference Earth model. Physics of

556   the earth and planetary interiors 25, 297-356.

557   Fee, D., Dueker, K., 2004. Mantle transition zone topography and structure beneath

558   the Yellowstone hotspot. Geophysical Research Letters 31.

559   Freitas, D., Manthilake, G., Chantel, J., Bouhifd, M., Andrault, D., 2019. Simultaneous

560   measurements of electrical conductivity and seismic wave velocity of partially

561   molten geological materials: effect of evolving melt texture. Physics and

562   Chemistry of Minerals, 1-17.

563   Gao, W., Matzel, E., Grand, S.P., 2006. Upper mantle seismic structure beneath eastern

564   Mexico determined from P and S waveform inversion and its implications.

565   Journal of Geophysical Research: Solid Earth 111.

566   Ghosh, S., Ohtani, E., Litasov, K., Suzuki, A., Sakamaki, T., 2007. Stability of carbonated

567   magmas at the base of the Earth's upper mantle. Geophysical research letters

568   34.

569   Guan, Z., Niu, F., 2017. An investigation on slowness-weighted CCP stacking and its

570   application to receiver function imaging. Geophysical Research Letters 44,

571   6030-6038.

572   Hier-Majumder, S., 2017, MuMaP_fwd-1.0, Version: (Version 1.0). Zenodo,

573   http://doi.org/10.5281/zenodo.1040971.

574   Hier-Majumder, S., Abbott, M.E., 2010. Influence of dihedral angle on the seismic

575   velocities in partially molten rocks. Earth and Planetary Science Letters 299, 23-

576   32.

577   Hier-Majumder, S., Courtier, A., 2011. Seismic signature of small melt fraction atop the

578   transition zone. Earth and Planetary Science Letters 308, 334-342.

579   Hier-Majumder, S., Keel, E.B., Courtier, A.M., 2014. The influence of temperature, bulk

580   composition, and melting on the seismic signature of the low-velocity layer

581   above the transition zone. Journal of Geophysical Research: Solid Earth 119,

582   971-983.

583   Hier-Majumder, S., Tauzin, B., 2017. Pervasive upper mantle melting beneath the

584   western US. Earth and Planetary Science Letters 463, 25-35.

585   Huckfeldt, M., Courtier, A.M., Leahy, G.M., 2013. Implications for the origin of

586   Hawaiian volcanism from a converted wave analysis of the mantle transition

587   zone. Earth and Planetary Science Letters 373, 194-204.

588   Jasbinsek, J., Dueker, K., 2007. Ubiquitous low-velocity layer atop the 410-km

589   discontinuity in the northern Rocky Mountains. Geochemistry, Geophysics,

590   Geosystems 8.

591   Jasbinsek, J.J., Dueker, K.G., Hansen, S.M., 2010. Characterizing the 410 km

592   discontinuity low-velocity layer beneath the LA RISTRA array in the North

593   American Southwest. Geochemistry, Geophysics, Geosystems 11.

594   Katsura, T., Yoneda, A., Yamazaki, D., Yoshino, T., Ito, E., 2010. Adiabatic temperature

595   profile in the mantle. Physics of the Earth and Planetary Interiors 183, 212-218.

596   Keifer, I., Dueker, K., 2019. Testing the hypothesis that temperature modulates 410

597   and 660 discontinuity topography beneath the eastern United States. Earth and

598   Planetary Science Letters 524, 115723.

599   Kennett, B., Engdahl, E., 1991. Traveltimes for global earthquake location and phase

600   identification. Geophysical Journal International 105, 429-465.

601   Mavko, G.M., 1980. Velocity and attenuation in partially molten rocks. Journal of

602   Geophysical Research: Solid Earth 85, 5173-5189.

603   Mei, S., Bai, W., Hiraga, T., Kohlstedt, D., 2002. Influence of melt on the creep behavior

604   of olivine–basalt aggregates under hydrous conditions. Earth and Planetary

605   Science Letters 201, 491-507.

606   Minarik, W.G., Watson, E.B., 1995. Interconnectivity of carbonate melt at low melt

607   fraction. Earth and Planetary Science Letters 133, 423-437.

608 Morra, G., Yuen, D.A., Boschi, L., Chatelain, P., Koumoutsakos, P., Tackley, P., 2010. The

609   fate of the slabs interacting with a density/viscosity hill in the mid-mantle.

610   Physics of the Earth and Planetary Interiors 180, 271-282.

611 Press, W.H., Teukolsky, S.A., Vetterling, W.T., Flannery, B.P., 2007. Numerical recipes

612   3rd edition: The art of scientific computing. Cambridge university press, p. 445.

613 Revenaugh, J., Sipkin, S., 1994. Seismic evidence for silicate melt atop the 410-km

614   mantle discontinuity. Nature 369, 474.

615 Richard, G.C., Bercovici, D., 2009. Water-induced convection in the Earth's mantle

616   transition zone. Journal of Geophysical Research: Solid Earth 114.

617 Schaeffer, A., Bostock, M., 2010. A low-velocity zone atop the transition zone in

618   northwestern Canada. Journal of Geophysical Research: Solid Earth 115.

619 Schmandt, B., Dueker, K., Hansen, S., Jasbinsek, J.J., Zhang, Z., 2011. A sporadic low-

620   velocity layer atop the western US mantle transition zone and short-

621   wavelength variations in transition zone discontinuities. Geochemistry,

622   Geophysics, Geosystems 12.

623 Song, T.-R.A., Helmberger, D.V., Grand, S.P., 2004. Low-velocity zone atop the 410-km

624   seismic discontinuity in the northwestern United States. Nature 427, 530.

625 Sun, Y., Hier-Majumder, S., Xu, Y., Walter, M., 2020. Stability and migration of slab-

626   derived carbonate-rich melts above the transition zone. Earth and Planetary

627   Science Letters 531, 116000.

628   Takei, Y., 1998. Constitutive mechanical relations of solid-liquid composites in terms of

629   grain-boundary contiguity. Journal of Geophysical Research: Solid Earth 103,

630   18183-18203.

631   Takei, Y., 2002. Effect of pore geometry on Vp/Vs: From equilibrium geometry to crack.

632   Journal of Geophysical Research: Solid Earth 107, 2043.

633   Tauzin, B., Debayle, E., Wittlinger, G., 2010. Seismic evidence for a global low-velocity

634   layer within the Earth's upper mantle. Nature Geoscience 3, 718.

635   Tauzin, B., Ricard, Y., 2014. Seismically deduced thermodynamics phase diagrams for

636   the mantle transition zone. Earth and Planetary Science Letters 401, 337-346.

637   Tauzin, B., Van Der Hilst, R.D., Wittlinger, G., Ricard, Y., 2013. Multiple transition zone

638   seismic discontinuities and low velocity layers below western United States.

639   Journal of Geophysical Research: Solid Earth 118, 2307-2322.

640   Thomson, A.R., Walter, M.J., Kohn, S.C., Brooker, R.A., 2016. Slab melting as a barrier

641   to deep carbon subduction. Nature 529, 76.

642   Vinnik, L., Farra, V., 2007. Low S velocity atop the 410-km discontinuity and mantle

643   plumes. Earth and Planetary Science Letters 262, 398-412.

644   Vinnik, L., Ren, Y., Stutzmann, E., Farra, V., Kiselev, S., 2010. Observations of S410p and

645   S350p phases at seismograph stations in California. Journal of Geophysical

646   Research: Solid Earth 115.

647   von Bargen, N., Waff, H.S., 1986. Permeabilities, interfacial areas and curvatures of

648   partially molten systems: results of numerical computations of equilibrium

649   microstructures. Journal of Geophysical Research: Solid Earth 91, 9261-9276.

650 Wimert, J., Hier-Majumder, S., 2012. A three-dimensional microgeodynamic model of

651   melt geometry in the Earth's deep interior. Journal of Geophysical Research:

652   Solid Earth 117.

653 Xiao, J., Waltham, D., 2019. Non-uniqueness and symmetry in stratigraphic

654   interpretations: A quantitative approach for determining stratal controls.

655   Sedimentology 66, 1700-1715.

656 Xu, W., Lithgow-Bertelloni, C., Stixrude, L., Ritsema, J., 2008. The effect of bulk

657   composition and temperature on mantle seismic structure. Earth and Planetary

658   Science Letters 275, 70-79.

659 Yoshino, T., Takei, Y., Wark, D.A., Watson, E.B., 2005. Grain boundary wetness of

660   texturally equilibrated rocks, with implications for seismic properties of the

661   upper mantle. Journal of Geophysical Research: Solid Earth 110.

662 Zhang, Z., Dueker, K.G., Huang, H.-H., 2018. Ps mantle transition zone imaging beneath

663   the Colorado Rocky Mountains: Evidence for an upwelling hydrous mantle.

664   Earth and Planetary Science Letters 492, 197-205.

665